

Floquet spectrum for anisotropic and tilted Dirac materials under linearly polarized light at all field intensities

Cite as: J. Appl. Phys. **127**, 234301 (2020); <https://doi.org/10.1063/5.0007576>

Submitted: 18 March 2020 . Accepted: 31 May 2020 . Published Online: 15 June 2020

J. C. Sandoval-Santana , V. G. Ibarra-Sierra , A. Kunold , and Gerardo G. Naumis 

COLLECTIONS

Paper published as part of the special topic on [Beyond Graphene: Low Symmetry and Anisotropic 2D Materials](#)

Note: This paper is part of the Special Topic on Beyond Graphene: Low Symmetry and Anisotropic 2D Materials.



View Online



Export Citation



CrossMark

ARTICLES YOU MAY BE INTERESTED IN

[Harmonic generation at the nanoscale](#)

Journal of Applied Physics **127**, 230901 (2020); <https://doi.org/10.1063/5.0006093>

[Tuning energy barriers by doping 2D group-IV monochalcogenides](#)

Journal of Applied Physics **127**, 234103 (2020); <https://doi.org/10.1063/5.0008502>

[High-efficiency electrically direction-controllable spoof surface plasmon polaritons coupler](#)

Journal of Applied Physics **127**, 233105 (2020); <https://doi.org/10.1063/1.5134976>

Lock-in Amplifiers
up to 600 MHz



Watch



Floquet spectrum for anisotropic and tilted Dirac materials under linearly polarized light at all field intensities

Cite as: J. Appl. Phys. **127**, 234301 (2020); doi: [10.1063/5.0007576](https://doi.org/10.1063/5.0007576)

Submitted: 18 March 2020 · Accepted: 31 May 2020 ·

Published Online: 15 June 2020



View Online



Export Citation



CrossMark

J. C. Sandoval-Santana,^{1,a)}  V. G. Ibarra-Sierra,^{2,b)}  A. Kunold,^{3,c)}  and Gerardo G. Naumis^{2,d)} 

AFFILIATIONS

¹Instituto de Física, Universidad Nacional Autónoma de México, Apartado Postal 20-364, 01000 Ciudad de México, México

²Departamento de Sistemas Complejos, Instituto de Física, Universidad Nacional Autónoma de México, Apartado Postal 20-364, 01000 Ciudad de México, México

³Área de Física Teórica y Materia Condensada, Universidad Autónoma Metropolitana Azcapotzalco, Av. San Pablo 180, Col. Reynosa-Tamaulipas, 02200 Ciudad de México, México

Note: This paper is part of the Special Topic on Beyond Graphene: Low Symmetry and Anisotropic 2D Materials.

^{a)}Electronic mail: jcarlooss@fisica.unam.mx

^{b)}Electronic mail: vickkun@fisica.unam.mx

^{c)}Electronic mail: akb@azc.uam.mx

^{d)}Author to whom correspondence should be addressed: naumis@fisica.unam.mx

ABSTRACT

The Floquet spectrum in an anisotropic tilted Dirac semimetal modulated by linearly polarized light is addressed through the solution of the time-dependent Schrödinger equation for the two-dimensional Dirac Hamiltonian via the Floquet theorem. The time-dependent wave functions and the quasienergy spectrum of the two-dimensional Dirac Hamiltonian under the normal incidence of linearly polarized waves are obtained for an arbitrarily intense electromagnetic radiation. We applied a set of unitary transformations to reduce the Schrödinger equation to an ordinary second-order differential Hill equation with complex coefficients. Through the stability analysis of this differential equation, the weak and strong field regimes are clearly distinguished in the quasi-spectrum. In the weak electric field regime, above a certain threshold given by the field parameters, the spectrum mostly resembles that of free electrons in graphene. Below this threshold, in the strong electric field regime, the spectrum abruptly becomes highly anisotropic and a gap opens up. As an example, we apply the results to the particular case of borophene.

Published under license by AIP Publishing. <https://doi.org/10.1063/5.0007576>

I. INTRODUCTION

The superior physical, mechanical, and chemical properties of two-dimensional (2D) materials make them an ideal playground to study new and exciting kinds of quantum phases.^{1–7} Their remarkable electronic and optical features have intensely driven the development of novel and innovative optoelectronic devices^{8–10} as broadband optical modulators,^{11–13} solar cells,^{14,15} infrared photo-detectors,¹⁶ and hybrid plasmonic devices.^{17,18}

In the last decade, persistent efforts have been made to harness the unique features of graphene's so-called dressed electrons^{8,16,19–27} to design different kinds of optoelectronic

devices. Now, it is well established that electromagnetic dressing, attained when electrons strongly couple to electromagnetic fields, substantially renormalize the energy and the velocities in graphene.^{19,27–29} In turn, renormalized parameters highly depend on the light polarization: in graphene, circularly polarized fields open a dynamical gap in the Dirac point, while linearly polarized fields leave it intact.²⁹ Particularly, dressed electrons under linearly polarized light induce an anisotropy of the electron dispersion relation.²⁶ Electromagnetic dressing could, therefore, be used to tune the electronic and optical properties of graphene, including band-gaps and carrier velocities,²⁷ which are clearly manifested in several

measurable physical properties as the photocurrent.^{23,30} A similar approach has been adopted in ultrafast material science promising optical and mechanical control of the physical properties of 2D materials.³¹ In this case, it is a time-dependent strain that acts as a pseudo-electromagnetic field.³²

In graphene, the weak-field regime, where light-matter coupling is perturbative,^{33–35} is well understood. It may be pictured as a quantized-photon field interacting with massless Dirac fermions having a conic dispersion relation. However, in the intense-field regime, this perturbative expansion cannot converge. The Dirac dispersion relation is highly distorted as a result of the electronic dressing rendering the quantized-photon picture invalid. It is clear then that this emerging field requires new theoretical tools that go beyond the conventional techniques.^{36,37} There are numerous proposals to approach this problem,^{19–22,24–26} but, even for graphene, some aspects of the interaction between carriers and strong time-driven fields remain elusive.

Another essential question that remains to be fully answered is how such an intense electromagnetic radiation would affect other Dirac materials^{38,39} as borophene or black-phosphorus,^{40–43} for example. Particularly, borophene is a remarkable anisotropic material.^{2,6,44,45} After being theoretically predicted 30 years ago,⁴⁶ it was until 2015 that it was synthesized.⁴⁷ Borophene turns out to be stronger and even more flexible than graphene. It is a good conductor of both electricity and heat, and it is expected to be a superconductor⁴⁸ with relatively high transition temperatures.

In a series of recent papers, we have investigated time-driven anisotropic Dirac Hamiltonians as the one that describes borophene.^{44,45,49,50} However, the mathematical complexity of the problem required several approximations that are only valid for very intense fields.^{45,50} Therefore, the critical link between weak fields, treatable with the perturbation theory, and strong fields is still missing. In particular, the cases of linearly and elliptically polarized light were studied in the intense-field regime,^{45,50} where the rather convoluted Hill equation with time dependent coefficients was simplified into the very well known Mathieu equation with constant coefficients. Nevertheless, the complete study of the Hill equation entails the interplay between the strong and weak field-intensity regimes, key to comprehend the formation of the quasienergy spectrum. This effect can be thoroughly studied by analyzing the quasi-energy spectrum using the Floquet theory.^{51–61}

In this paper, we address the general problem of a particle that obeys the anisotropic Dirac Hamiltonian subject to linearly polarized light with an arbitrarily large field intensity. The calculation of the quasienergy spectrum and the wave function is achieved through a set of unitary transformations that enable reducing the matrix differential equation into a scalar differential equation. This, in turn, is readily solved via the Floquet theorem and a Fourier spectral decomposition of the periodical part of the solution. It is shown that in the intense field regime, the quasienergy spectrum abruptly develops an anisotropic structure, absent in the weak field regime.

Finally, it is important to put our present findings in the context of earlier studies made by other authors. Most of the interest has been placed in Dirac or Weyl Hamiltonians without tilting, and for these cases, perturbative methods were used to find the Floquet spectrum.^{28,29} Here, we show an analytic expression valid for all field intensities, as it was made for graphene many years

ago.¹⁹ The strong anisotropy reported here for borophene cannot be obtained by usual perturbation techniques.

The paper is organized as follows. In Sec. II, we introduce the low-energy effective two-dimensional anisotropic Dirac Hamiltonian, and we study the case of borophene subject to an arbitrarily intense linearly polarized electromagnetic field. Subsequently, in Sec. III, we analyze the quasienergy spectrum that emerges from the Hill equation by means of the Floquet approach. Also, we find the time-dependent wave functions. Finally, we summarize and conclude in Sec. IV.

II. TWO-DIMENSIONAL ELECTRONS IN A TILTED DIRAC CONE SUBJECT TO ELECTROMAGNETIC FIELDS

A. The anisotropic Dirac Hamiltonian

We start by considering a low-energy anisotropic Dirac Hamiltonian close to one of the Dirac points. In the particular case of 8-*Pmmn* borophene, it is given by^{44,45,49,62}

$$\hat{H} = \hbar v_t k_y \hat{\sigma}_0 + \hbar [v_x k_x \hat{\sigma}_x + v_y k_y \hat{\sigma}_y], \quad (1)$$

where k_x and k_y are the components of the two-dimensional momentum vector \mathbf{k} , $\hat{\sigma}_x$ and $\hat{\sigma}_y$ are the Pauli matrices, and $\hat{\sigma}_0$ is the 2×2 identity matrix. The three velocities in the anisotropic 8-*Pmmn* borophene Dirac Hamiltonian (1) are given by $v_x = 0.86 v_F$, $v_y = 0.69 v_F$, and $v_t = 0.32 v_F$, where $v_F = 10^6$ m/s⁴⁹ is the Fermi velocity. In Eq. (1), the last two terms give rise to the familiar form of the kinetic energy, leading to the Dirac cone and the first one tilts the Dirac cone in the k_y direction. These two features are contained in the energy dispersion relation,⁵⁰

$$E_{\nu, \mathbf{k}} = \left(\frac{v_t}{v_y} \right) \tilde{k}_y + \nu \varepsilon, \quad (2)$$

where

$$\varepsilon = \sqrt{\tilde{k}_x^2 + \tilde{k}_y^2}, \quad (3)$$

and $\nu = \pm 1$ is the band index. In Eq. (2), we used the set of renormalized moments $\tilde{k}_x = \hbar v_x k_x$, $\tilde{k}_y = \hbar v_y k_y$. The corresponding free electron wave function is

$$\psi_{\nu}(\mathbf{k}) = \frac{1}{\sqrt{2}} \begin{bmatrix} 1 \\ \nu \exp(i\theta_{\mathbf{k}}) \end{bmatrix}, \quad (4)$$

where $\theta_{\mathbf{k}} = \tan^{-1}(\tilde{k}_y/\tilde{k}_x)$.

B. Linearly polarized waves

Now, we consider a charge carrier, described by the two-dimensional anisotropic Dirac Hamiltonian, subject to an electromagnetic wave that propagates along a direction perpendicular to the surface of the crystal. The effects of the electromagnetic field are introduced in the Hamiltonian (1) through the Peierls substitution⁶³ $\hbar \mathbf{k} \rightarrow \hbar \mathbf{k} - e\mathbf{A}$, where $\mathbf{A} = (A_x, A_y)$ is the vector potential of the electromagnetic wave. A considerable simplification can be achieved

by adopting a gauge in which \mathbf{A} only depends on time. The Hamiltonian (1) is thus transformed into

$$\hat{H} = \frac{v_t}{v_y} \left(\tilde{k}_y - ev_y A_y \right) \hat{\sigma}_0 + \left(\tilde{k}_x - ev_x A_x \right) \hat{\sigma}_x + \left(\tilde{k}_y - ev_y A_y \right) \hat{\sigma}_y. \quad (5)$$

In principle, in the expression above, the polarization can be linear, circular, or elliptical. Although the cases of circularly or elliptically polarized light are very interesting, the nature of the solution presented here is much more involved for these cases. The reason is that linear polarization breaks the spatial symmetry. This is not the case for other kinds of polarizations, and thus, the transformations proposed here are strongly modified. However, from results in other 2D materials in the weak field regime using perturbation approaches, we can expect a gap opening.^{28,29} Assuming that the electromagnetic wave is linearly polarized, the vector potential can be written as

$$\mathbf{A} = \frac{E_0}{\Omega} \cos(\Omega t) \hat{\mathbf{r}}, \quad (6)$$

where $\hat{\mathbf{r}} = (1, 0)$ is the polarization vector, E_0 is the uniform amplitude of the electric field, and Ω is the angular frequency of the electromagnetic wave. Observe that here, the field \mathbf{A} is not quantized and is treated classically. Thus, our results are valid for a field with a large number of photons, which can be represented by a quantum coherent field.

In the Schrödinger equation corresponding to (5),

$$i\hbar \frac{d}{dt} \Psi(t) = \hat{H} \Psi(t), \quad (7)$$

the two-dimensional spinor can be expressed as $\Psi(t) = (\Psi_A(t), \Psi_B(t))^T$, where A and B label the two sublattices.

The main difficulty in deducing the wave function's explicit form resides in that the Hamiltonian (5) couples the differential equations for the $\Psi_A(t)$ and $\Psi_B(t)$ spinor components due to the terms that are proportional to $\hat{\sigma}_x$ and $\hat{\sigma}_y$. To uncouple the spinor components, we proceed as follows. First, applying a 45° rotation around the k_y axis of the form

$$\Psi(t) = \exp \left[-\frac{i}{\hbar} \left(\frac{\pi}{4} \right) \hat{\sigma}_y \right] \Phi(t) \quad (8)$$

conveniently transforms the non-diagonal $\hat{\sigma}_x$ matrix into $\hat{\sigma}_z$. Indeed, substituting (8) into Eq. (7) yields

$$i \frac{d}{d\phi} \Phi(\phi) = \frac{2}{\hbar\Omega} \left[\left(\frac{v_t}{v_y} \right) \tilde{k}_y \hat{\sigma}_0 + \tilde{\Pi}_x \hat{\sigma}_z + \tilde{k}_y \hat{\sigma}_y \right] \Phi(\phi), \quad (9)$$

where the only non-diagonal remaining term is the one proportional to $\hat{\sigma}_y$. In the foregoing equation, $\phi = \Omega t/2$, $\tilde{\Pi}_x = \tilde{k}_x - \zeta_x \cos(2\phi)$, and $\zeta_x = ev_x E_x / \Omega$. The spinor components of $\Phi(\phi) = (\Phi_+(\phi), \Phi_-(\phi))^T$ are given by $\Phi_+(\phi) = [\Psi_A(\phi) + \Psi_B(\phi)]/\sqrt{2}$ and $\Phi_-(\phi) = [\Psi_A(\phi) - \Psi_B(\phi)]/\sqrt{2}$. Second, the term

proportional to $\hat{\sigma}_0$ in Eq. (9) is removed by adding a time-dependent phase to the wave function,

$$\Phi(\phi) = \exp \left[-2i \left(\frac{v_t}{v_y} \right) \frac{\tilde{k}_y}{\hbar\Omega} \phi \hat{\sigma}_0 \right] \chi(\phi), \quad (10)$$

where $\chi(\phi) = (\chi_{+1}(\phi), \chi_{-1}(\phi))^T$. Finally, after inserting Eq. (10) into Eq. (9), we follow the procedure shown in Appendix A of Ref. 50. The resulting differential equation takes on the form of the Hill equation,⁶⁴

$$\chi''(\phi) + \mathbb{F}(\phi)\chi(\phi) = 0, \quad (11)$$

where the matrix $\mathbb{F}(\phi)$ is defined as

$$\mathbb{F}(\phi) = [a + q_1 \cos(2\phi) + q_2 \cos(4\phi)] \hat{\sigma}_0 + q_3 \sin(2\phi) \hat{\sigma}_z. \quad (12)$$

The Hill equation parameters,

$$a = \left(\frac{2\varepsilon}{\hbar\Omega} \right)^2 + q_2, \quad (13)$$

$$q_1 = -4\sqrt{2}q_2 \left(\frac{\tilde{k}_x}{\hbar\Omega} \right), \quad (14)$$

$$q_3 = 2i\sqrt{2}q_2, \quad (15)$$

where q_2 is given by

$$q_2 = 2 \left(\frac{\zeta_x}{\hbar\Omega} \right)^2, \quad (16)$$

are expressed in terms of the ratios of the characteristic energies of the system. Thereby, $\varepsilon/\hbar\Omega$ is the ratio of the electron kinetic energy to the photon energy, $\zeta_x/\hbar\Omega$ is the ratio of the work done on the charged carriers by the electromagnetic wave to the photon energy, and $\tilde{k}_x/\hbar\Omega$ is the ratio of the x part of the electron kinetic energy to the photon energy.

Expressing (11) as a second-order differential equation is quite advantageous for the calculations that follow. First, the evolution operator that propagates the state χ in time must be diagonal since $\mathbb{F}(\phi)$ is solely composed of the diagonal matrices $\hat{\sigma}_0$ and $\hat{\sigma}_z$. As a consequence of this, the scalar differential equations for the $\chi_{+1}(\phi)$ and $\chi_{-1}(\phi)$ spinor components decouple. Moreover, the differential equation for the $\chi_{-1}(\phi)$ component turns out to be the complex conjugate of the one for $\chi_{+1}(\phi)$. Both differential equations may be summarized by

$$\chi''_{\eta}(\phi) + [a + q_1 \cos(2\phi) + q_2 \cos(4\phi) + \eta q_3 \sin(2\phi)] \chi_{\eta}(\phi) = 0, \quad (17)$$

where $\eta = \pm 1$.

This alternative form of the Schrödinger equation considerably simplifies the computation and analysis of the stability spectrum.

III. QUASIENERGY SPECTRUM AND WAVE FUNCTION

A. Quasienergy spectrum

In this section, we analyze the quasienergy spectrum produced by the Hill equation (17) and its relations with the stability of its solutions. The determination of the stability regions of this differential equation is quite challenging mainly due to the imaginary coefficient q_3 . The real coefficients a , q_1 , and q_2 alone give rise to the Whittaker–Hill equation,⁶⁵ widely discussed in the spectral theory of periodic differential equations. The imaginary coefficient q_3 , however, introduces additional difficulties that are rarely addressed in the literature.⁶⁶ Among other things, it yields complex characteristic values. Despite the added complexity, Eq. (17) may be approached by Whittaker's original assumption^{64,67} that the solution should take the Floquet normal form

$$\chi_\eta(\phi) = \exp[i\mu_\eta\phi]u_\eta(\phi) \quad (18)$$

due to the periodicity of the Hamiltonian. Also, according to the Floquet theorem, $u_\eta(\phi)$ must be a function with the period π . The function $\mu_\eta(a)$ is termed the characteristic exponent. As detailed in Sec. III B, the characteristic exponent and the quasienergy spectrum are closely connected. Thanks to the periodicity of the $u_\eta(\phi)$ function, $\chi_\mu(\phi)$ might be expressed as a Fourier series expansion. In this manner, the second-order differential equation with time-variable periodic coefficients is traded for a matrix eigenvalue problem. The eigenvalues that stem from it are precisely the characteristic exponents $\mu_\eta(a)$. These have the form

$$\mu_\eta(a) = \frac{1}{\pi} \cos^{-1} [1 + \Delta_\eta(0)(\cos(\sqrt{a}\pi) - 1)], \quad (19)$$

where a and $\Delta_\eta(0)$ are given by Eqs. (13) and (9), respectively. For a detailed calculation of $\mu_\eta(a)$, refer to the Appendix.

In general, the solutions of the Hill equation (17) fall either on stable ($\text{Im}[\mu_\eta(a)] = 0$) or unstable regions ($\text{Im}[\mu_\eta(a)] \neq 0$) depending on the values taken by the coefficients a , q_1 , q_2 , and q_3 provided they are being considered as independent parameters.^{65–67} Furthermore, if we chart the stable and unstable regions in the $(a, \zeta_x/\hbar\Omega)$ domain, the resulting stability diagram greatly resembles that of the Mathieu differential equation. Surprisingly, all the physical solutions fall on the stable regions when these coefficients are restricted by the parametrization of Eqs. (13)–(15) for seemingly arbitrary domain spaces of \tilde{k}_x , \tilde{k}_y , and ζ_x . The mathematical reason behind the stability comes from the extra relationships that exist between parameters. By looking at the definitions of a , q_1 , q_2 , and q_3 , it is clear that once q_2 is given, only ε and \tilde{k}_x remain as free parameters. Yet, these two are related by the dispersion equation (3). Thus, there are extra constraints that reduce the space of possible solutions when compared with a stability diagram made by considering independent parameters. Physically, such relations between parameters arise as a consequence of energy-momentum conservation. As an example, consider Eq. (13) in the limit where $\varepsilon/\hbar\Omega \gg \sqrt{q_2}$. Thus, $a \gg q_2$ from where it follows that

$$\frac{2\varepsilon}{\hbar\Omega} = \sqrt{a - q_2} \approx \sqrt{a} \left(1 - \frac{q_2}{2a}\right). \quad (20)$$

At the same time, the condition $\varepsilon/\hbar\Omega \gg \sqrt{q_2}$ implies by the dispersion relationship that along the x-axis, $k_x/\hbar\Omega \gg \sqrt{q_2}$, and by Eqs. (14)–(16), $|q_1| \gg q_2, |q_3|$. In this limit, Eq. (17) can be reduced to the Mathieu equation where gaps occur for $\sqrt{a} \approx n$ for an integer n . Therefore, Eq. (20) represents a dressed valence to conduction band transition, as for $q_2 \rightarrow 0$, we recover the energy conservation $2\varepsilon \approx n\hbar\Omega$ of photon absorption by the electron. This limiting case is obtainable from simple perturbation techniques. In the Floquet theory, the extra q_2 term results from the electron-dressing and keeps the transition slightly away from the resonance-gap opening condition.

We have, therefore, numerically determined the stability diagram of the Hill equation in the $(a, \zeta_x/\hbar\Omega)$ -plane and systematically confirmed that the parametrization given by Eqs. (13)–(15) indeed falls in the stability region. Figure 1 shows a density plot of the characteristic exponent spectrum for $\mu_{+1}(a)$ as a function of the normalized momenta $k_x/\hbar\Omega$ and $k_y/\hbar\Omega$. Over the entire parameter space covered in this figure, the solutions of the Hill equation are stable.

One of the most striking features of the spectrum emerges when one compares the quasienergies at low, intermediate, and high electric field amplitudes. The contrast between the effects of weak ($E_x = 10^{-4}$ V/m, $\zeta_x/\hbar\Omega = 10^{-3}$), intermediate ($E_x = 4.85$ V/m, $\zeta_x/\hbar\Omega = 2.5$), and strong ($E_x = 9.7$ V/m, $\zeta_x/\hbar\Omega = 5$) electric field amplitudes is shown in Figs. 1(a)–1(c), respectively. In the weak electric field regime [see Fig. 1(a)], the isolines of the characteristic exponent $\mu_{+1}(a)$ as a function of the normalized momenta form a pattern of concentric circles. In the intermediate electric field regimes [see Fig. 1(b)], a spectrum of vertical lines, perpendicular to the electric field direction, emerges close to the Dirac point ($\tilde{k}_x = \tilde{k}_y = 0$). The vertical grill is surrounded by an elliptical outline that is approximately delimited by the white circle of radius $\varepsilon = \zeta_x$. In the vicinity of this contour ($\varepsilon > \zeta_x$), the spectrum takes on an elliptical form but further out ($\varepsilon \gg \zeta_x$), the spectrum recovers the circular shape observed in the low electric field regime. For intense electric fields, the spectrum has the same overall behavior as the intermediate case. The main difference is the radius of the white circle and the number of vertical lines, which are increased in the strong field case.

The appearance of the vertical grill in the quasienergy spectrum is due to the interplay between the terms $\cos(2\phi)$, $\sin(2\phi)$, and $\cos(4\phi)$ in Eq. (17). For example, $\varepsilon < \zeta_x$ implies that $q_2 > |q_3|$ and $|q_3| > q_1$; therefore, the most significant term is $\cos(4\phi)$. By contrast, $\varepsilon > \zeta_x$ implies that $q_1 > |q_3|$ and $|q_3| > q_1$, and the dominant element is $\cos(2\phi)$.

Further details of the spectrum are appreciated in Fig. 2 where we show a 3D plot of the quasienergy $\mu_{+1}(a)$ as a function of k_x and k_y in the high electric field regime ($\zeta_x/\hbar\Omega = 5$).

B. Wave function and the Floquet spectrum

As mentioned above, the wave function in (7) must satisfy the Floquet theorem as a result of the time periodicity of the Hamiltonian (5). Hence, following the Floquet theorem, Eqs. (8), (10), and (18) can be combined into the wave function,

$$\Psi(\phi) = \mathcal{N} \exp\left[-\frac{i}{\hbar} \left(\frac{\pi}{4}\right) \hat{\sigma}_y\right] \mathcal{U}(\phi)\chi(0), \quad (21)$$

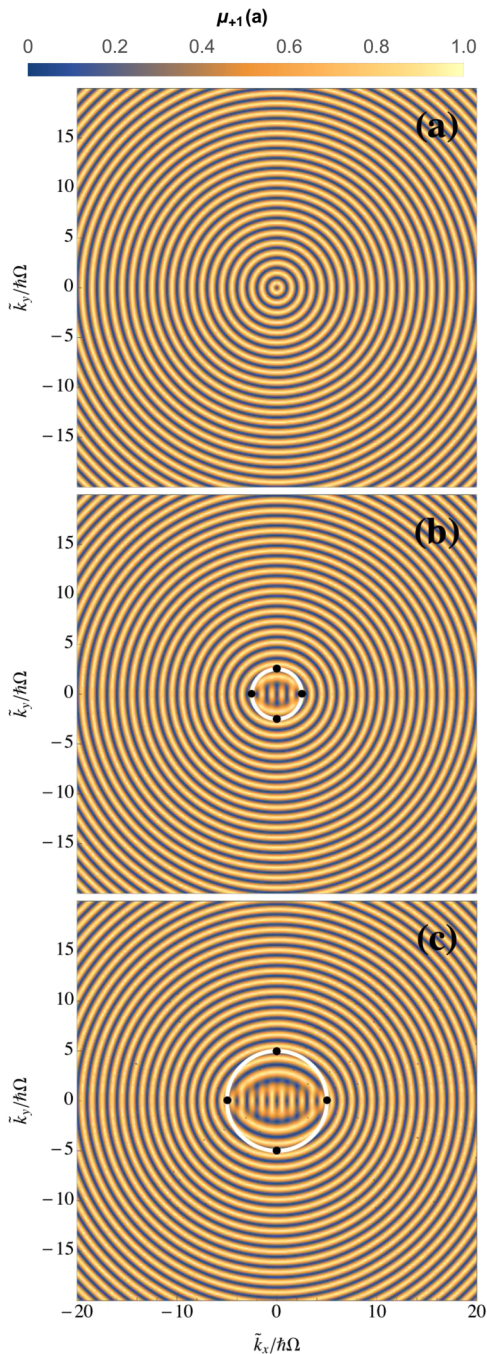


FIG. 1. Density plot of the characteristic exponent spectrum $\mu_{+1}(a)$ as a function of $\tilde{k}_x/h\Omega$ and $\tilde{k}_y/h\Omega$ for (a) $\zeta_x/h\Omega = 10^{-3}$ with $E_x = 10^{-4}$ V/m, (b) $\zeta_x/h\Omega = 2.5$ with $E_x = 4.85$ V/m, and (c) $\zeta_x/h\Omega = 5$ with $E_x = 9.7$ V/m. In all cases, the frequency of the electromagnetic field has a value $\Omega = 50 \times 10^9$ Hz. The white circle indicates the theoretical threshold given by the radius $\varepsilon = \zeta_x$ at which there is a transition from a field-driven strong to weak anisotropy solution. The black dots denote the limits of the white circle in the cases where $\tilde{k}_x/h\Omega = 0$ and $\tilde{k}_y/h\Omega = 0$.

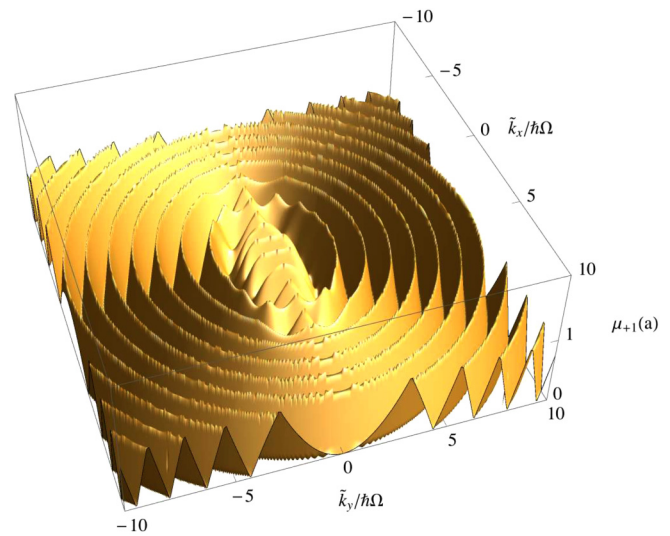


FIG. 2. Characteristic exponent spectrum $\mu_{+1}(a)$ as a function of the normalized momenta $\tilde{k}_x/h\Omega$ and $\tilde{k}_y/h\Omega$ in the intense electric field regime. This plot was made for $\zeta_x/h\Omega = 5$ with $E_x = 9.7$ V/m and $\Omega = 50 \times 10^9$ Hz.

where \mathcal{N} is a normalization constant, $\chi(0) = (\chi_{+1}(0), \chi_{-1}(0))^T$ is the initial state vector in (17), and $\mathcal{U}(\phi)$ denotes the time evolution operator such that $\chi(\phi) = \mathcal{U}(\phi)\chi(0)$. As we pointed out before, because $\mathbb{F}(\phi)$ is a diagonal matrix, the evolution operator must also be diagonal. Thus, it can be expressed quite generally as

$$\mathcal{U}(\phi) = \begin{pmatrix} \exp[-i\varepsilon_{+1}\phi]u_{+1}(\phi) & 0 \\ 0 & \exp[-i\varepsilon_{-1}\phi]u_{-1}(\phi) \end{pmatrix}, \quad (22)$$

where $u_{-1}(\phi) = u_{+1}^*(\phi)$ has the period π , and

$$\varepsilon_\eta = 2 \frac{v_t \tilde{k}_y}{v_y \hbar \Omega} + \mu_\eta(a). \quad (23)$$

It is easy to verify that the wave function (21) reduces to the free-particle wave function (4) when the electric field vanishes. From the Floquet theory,^{68–71} the time evolution operator is periodic $\mathcal{U}(\phi) = \mathcal{U}(\phi + l\pi)$, and quasienergy can be expressed as

$$\mathcal{E}_{\eta,l} = \varepsilon_\eta + l = 2 \frac{v_t \tilde{k}_y}{v_y \hbar \Omega} + \mu_{\eta,l}(a), \quad (24)$$

where

$$\mu_{\eta,l}(a) = \mu_\eta(a) + l, \quad l \in \mathbb{Z} \quad (25)$$

is the characteristic exponent for different Brillouin zones, which are tagged by the integer subscript l .

In Fig. 3, we show the quasienergy for $\mathcal{E}_{+1,0}$. At the bottom of this figure, a density plot of $\mu_{+1,0}(a)$ is shown for reference. One notes that the spectrum consists of the quasienergies $\mu_{+1}(a)$, plotted in Fig. 2, onto the tilt that comes from the first term of

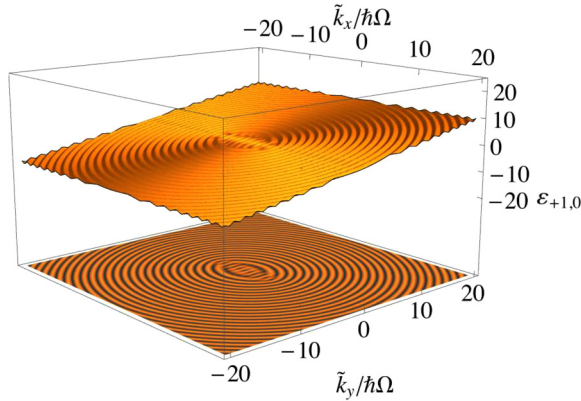


FIG. 3. Quasienergy $\mathcal{E}_{+1,0}$ spectrum as a function of the normalized momenta $\tilde{k}_x/\hbar\Omega$ and $\tilde{k}_y/\hbar\Omega$ in the strong electric field regime ($\zeta_x/\hbar\Omega = 5$, $E_x = 9.7$ V/m) for $\Omega = 50 \times 10^9$ Hz. The density plot at the bottom of the plot is a projection of the 3D plot at the top (see 1(b)).

Eq. (24). It arises from the anisotropic character of the Hamiltonian (1). Even though it strongly distorts the symmetry of the Dirac cone, it has been shown that interband transitions are not affected by it in the zero-temperature limit.⁶²

Different cross sections of the quasienergy spectrum $\mu_{\eta,l}(a)$ are shown in Fig. 4 for the Brillouin zones $l = -1, 0, 1$. Panels (a) and (b) show the spectrum section planes $\tilde{k}_y = 0$ and $\tilde{k}_x = 0$, respectively, in the weak electric field regime ($\zeta_x/\hbar\Omega = 10^{-3}$, $E_x = 10^{-3}$ V/m, and $\Omega = 50 \times 10^9$ Hz). In this case, both $\tilde{k}_y = 0$ and $\tilde{k}_x = 0$ cross sections are almost identical since the electric field is not intense enough to provoke any distortion to the free-particle spectrum. The quasienergies for the many Brillouin zones as functions of \tilde{k}_x [panel (a)] or \tilde{k}_y [panel (b)] have the form of a triangular function. In the intermediate electric field regime ($\zeta_x/\hbar\Omega = 2.5$, $E_x = 4.85$ V/m, and $\Omega = 50 \times 10^9$ Hz) and the strong electric field regime ($\zeta_x/\hbar\Omega = 5$, $E_x = 9.7$ V/m, and $\Omega = 50 \times 10^9$ Hz), both cuts are radically different. In panel (c) for intermediate and (e) for strong electric fields, we note that the $\tilde{k}_y = 0$ cross section of the spectrum resembles those corresponding to the weak electric field regime also exhibiting a triangular shaped function of \tilde{k}_x . However, in the $\tilde{k}_x = 0$ panels [panels (d) and (f)], the presence of the electromagnetic field becomes evident as the spectrum is warped approximately in the domain $-1 < \tilde{k}_y < 1$ for intermediate and $-2 < \tilde{k}_y < 2$ for strong electric fields. At both ends of this range, the quasienergy abruptly recovers the triangular feature that characterizes the spectrum in the absence of electromagnetic radiation. This distortion is roughly bounded by the two black vertical lines that correspond to the black dots in Figs. 1(b) and 1(c) where the strength of the electromagnetic field is comparable to the energy of the unperturbed system; i.e., $\varepsilon = \zeta_x$. A quite robust feature of the spectrum is the preservation of the gapless Dirac cone in the vicinity of the Dirac point: the quasienergies $\mu_{+1,l}$ and $\mu_{-1,l}$ as well as $\mathcal{E}_{+1,l}$ and $\mathcal{E}_{-1,l}$ touch at the tip of the Dirac point despite the intensity of the linearly polarized electromagnetic field. Nevertheless, the conic dispersion relation is stretched along

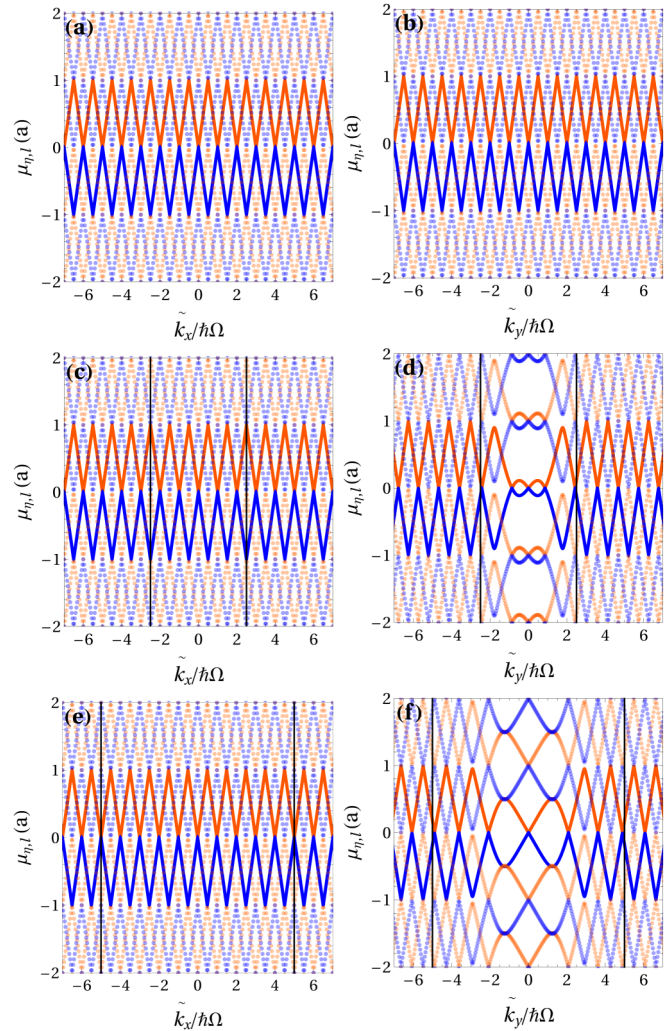


FIG. 4. Section planes of the quasienergy $\mu_{\eta,l}(a)$ as a function of $\tilde{k}_x/\hbar\Omega$ or $\tilde{k}_y/\hbar\Omega$ for the Brillouin zones $l = -1, 0, 1$. Panels (a) and (b) correspond to the weak electric field regime ($\zeta_x/\hbar\Omega = 10^{-3}$ and $E_x = 10^{-3}$ V/m). The intermediate electric field regime ($\zeta_x/\hbar\Omega = 2.5$ and $E_x = 4.85$ V/m) is shown in panels (c) and (d). The strong electric field regime ($\zeta_x/\hbar\Omega = 5$ and $E_x = 9.7$ V/m) is shown in panels (e) and (f). In all cases, the frequency of the electromagnetic field has a value of $\Omega = 50 \times 10^9$ Hz. The solid orange and blue lines correspond to the quasienergies $\mu_{+1,0}(a)$ and $\mu_{-1,0}(a)$, respectively. The light dots plot the quasienergy $\mu_{\pm 1, \pm 1}(a)$ in the adjacent Brillouin zones ($l = \pm 1$). The threshold $\varepsilon = \zeta_x$, where the energy of the electric field ζ_x is identical to the unperturbed energy ε , is indicated by the vertical black lines in panels (c) and (d).

the \tilde{k}_y direction as a result of the renormalization of the v_y component of the velocity due to electronic dressing. Despite the absolute absence of a gap at the tip of the Dirac cone, it is possible to open up gaps in other zones of the spectrum. In Fig. 4(d), the appearance of a small gap between $\mu_{+1,l}$ and $\mu_{-1,l}$ can be appreciated at $\tilde{k}_y/\hbar\Omega \approx \pm 2$.

Finally, as an experimental layout to observe the results presented in this work, we propose to use borophene over a dielectric substrate like SiO₂ or h-BN. Like in graphene experiments that measure induced photocurrents,^{33,72} a Ti:sapphire laser (650–1100 nm) is the most convenient. Using this electromagnetic wave source with a frequency $\Omega = 1713$ THz and powers per unit area of $6.7 \times 10^{-9} \text{ W/nm}^2 \leq P \leq 0.2 \text{ W/nm}^2$, corresponding to the field strength in the interval of $0.02 \text{ V/nm} \leq E_x \leq 11.23 \text{ V/nm}$, it should be possible to find the spectra of Fig. 1 with $10^{-3} < (\zeta_x/\hbar\Omega) < 5$.

IV. CONCLUSIONS

We investigated the quasienergy spectrum of an anisotropic tilted Dirac material subject to an arbitrarily intense linearly polarized electromagnetic field. To this end, we studied the behavior of 8-*Pmmn* borophene under the normal incidence of a linearly polarized field. We worked out the time-dependent wave function and the quasienergy spectrum from the Schöndinger equation via the Floquet theory. The quasienergy spectrum exhibits a sharp difference between the weak and strong electromagnetic field regimes. While in the first, the quasienergy as a function of the quasimomenta (k_x and k_y) is highly isotropic, the latter presents an anisotropic pattern in the low-energy region that resembles a grid aligned perpendicularly to the direction of the radiation's electric field. This pattern abruptly disappears beyond the threshold where the free kinetic energy of the carriers is larger than the energy associated with the electric field. Near this threshold, a gap opens up. Probably, the most astonishing feature of this spectrum is that, even though the gapless Dirac cone is preserved, the dispersion relation is stretched along the direction perpendicular to the field's polarization. This is an outcome of the electronic dressing and the consequent rescaling of the velocity. This mechanism could be exploited to tune the electronic properties of Dirac materials through the field parameters. A fundamental aspect, yet to be addressed, is the capability of circularly polarized fields to adjust these properties.

The potential of electron dynamics direction-control using irradiation has many interesting potential applications. For example, in combination with other semiconductors, graphene has proven to be a good platform to build polarization-sensitive photodetectors.⁷³ Our results suggest that in 2D Dirac materials, the photoconductivity must be strongly influenced by the polarization direction as a consequence of the quasi-spectrum orientation. This property, along with the large mobility presented by these materials, could be exploited to overcome the limitations of the most common polarimeter architectures that either limit compactness,⁷⁴ spatial,⁷⁵ or temporal resolution.^{73,76} One can thus envision graphene or borophene based fast and monolithic linear polarization-sensitive photodetectors. Moreover, it is known that under circularly polarized light, 2D materials exhibit the formation of a dynamical gap in the Dirac point²⁷ (not addressed in this paper). This could extend the sensing capabilities of 2D Dirac materials to circularly polarized light.

AUTHORS' CONTRIBUTIONS

All authors contributed equally to this work.

ACKNOWLEDGMENTS

This work was supported by DCB UAM-A Project CB009-19 and UNAM DGAPA PAPIIT (No. IN102620). J.C.S.-S. and V.G.I.-S. acknowledge the total support from the DGAPA-UNAM fellowship.

APPENDIX: WHITTAKER METHOD TO FIND THE CHARACTERISTIC EXPONENTS

This appendix covers the method developed by Whittaker^{64,67} to determine the characteristic exponent (19). Equation (17) is the starting point. This equation is periodic, and therefore, its solution must comply with the Floquet theorem. Thus, the solution is given by

$$\chi_\eta(\phi) = e^{i\mu_\eta\phi} u_\eta(\phi), \quad (\text{A1})$$

where $\eta = \pm 1$, $u_\eta(\phi)$ is a function with the period π and μ_η denotes the characteristic exponent. Thanks to the periodicity of $u_\eta(\phi)$, the wave function can be expanded as a Fourier series as

$$\chi_\eta(\phi) = e^{i\mu_\eta\phi} \sum_{r=-\infty}^{\infty} C_{2r}^{(\eta)} e^{i2r\phi}. \quad (\text{A2})$$

Substituting the preceding equation into (17) and rearranging the coefficients, we obtain the following recurrence relation:

$$\gamma_{2r} C_{2(r-2)}^{(\eta)} + \alpha_{2r} C_{2(r-1)}^{(\eta)} + C_{2r}^{(\eta)} + \beta_{2r} C_{2(r+1)}^{(\eta)} + \gamma_{2r} C_{2(r+2)}^{(\eta)} = 0, \quad (\text{A3})$$

where

$$\alpha_{2r} = \frac{1}{2} \frac{q_1 - i\eta q_3}{a - (\mu + 2r)^2}, \quad (\text{A4})$$

$$\beta_{2r} = \frac{1}{2} \frac{q_1 + i\eta q_3}{a - (\mu + 2r)^2}, \quad (\text{A5})$$

$$\gamma_{2r} = \frac{1}{2} \frac{q_2}{a - (\mu + 2r)^2}. \quad (\text{A6})$$

The equation parameters a , q_1 , q_2 , and q_3 are defined in Eqs. (13)–(15). The recurrence relation (3) can be put in the form of a linear equation as

$$\mathcal{A}_r(\mu, \eta, a, q_1, q_2, q_3) C^{(\eta)} = 0, \quad (\text{A7})$$

where $\mathbf{C}^{(\eta)} = (C_2^{(\eta)}, C_4^{(\eta)}, C_6^{(\eta)}, \dots)^\top$ and

$$\mathcal{A}_r(0, \eta, a, q_1, q_2, q_3) = \begin{pmatrix} 1 & \alpha_{2r} & \gamma_{2r} & 0 & 0 & 0 & 0 & 0 & 0 \\ \beta_{2r-2} & \cdot & 0 \\ 0 & \cdot & 1 & \alpha_4 & \gamma_4 & 0 & 0 & \cdot & 0 \\ 0 & \cdot & \beta_2 & 1 & \alpha_2 & \gamma_2 & 0 & \cdot & 0 \\ 0 & \cdot & \gamma_0 & \beta_0 & 1 & \alpha_0 & \gamma_0 & \cdot & 0 \\ 0 & \cdot & 0 & \gamma_{-2} & \beta_{-2} & 1 & \alpha_{-2} & \cdot & 0 \\ 0 & \cdot & 0 & 0 & \gamma_{-4} & \beta_{-4} & 1 & \cdot & 0 \\ 0 & \cdot & \alpha_{-2r+2} \\ 0 & 0 & 0 & 0 & 0 & 0 & \gamma_{-2r} & \beta_{-2r} & 1 \end{pmatrix}. \quad (\text{A8})$$

To avoid the trivial solution, we demand that the determinant of the precedent matrix vanishes,

$$\Delta_\eta(0) = \det[\mathcal{A}_r(0, \eta, a, q_1, q_2, q_3)] = 0. \quad (\text{A9})$$

It can be proven that this determinant may be written in the compact form,⁶⁷

$$\sin^2\left(\mu_\eta(a)\frac{\pi}{2}\right) = \Delta_\eta(0) \sin^2\left(\sqrt{a}\frac{\pi}{2}\right). \quad (\text{A10})$$

Solving the above equation for $\mu_\eta(a)$, we obtain

$$\mu_\eta(a) = \frac{1}{\pi} \cos^{-1} [1 + \Delta_\eta(0)(\cos(\sqrt{a}\pi) - 1)]. \quad (\text{A11})$$

This expression presents the advantage of being efficiently evaluated by using numerical methods. Strictly speaking, \mathcal{A}_r is infinite-dimensional; however, good numerical convergence of $\mu_\eta(a)$ is achieved by cutting it down to a 400×400 matrix.

DATA AVAILABILITY

The data that support the findings of this study are available from the corresponding author upon reasonable request.

REFERENCES

- ¹K. S. Novoselov, V. Fal, L. Colombo, P. Gellert, M. Schwab, K. Kim *et al.*, "A roadmap for graphene," *Nature* **490**, 192 (2012).
- ²B. Peng, H. Zhang, H. Shao, Y. Xu, R. Zhang, and H. Zhu, "The electronic, optical, and thermodynamic properties of borophene from first-principles calculations," *J. Mater. Chem. C* **4**, 3592–3598 (2016).
- ³T. Wehling, A. M. Black-Schaffer, and A. V. Balatsky, "Dirac materials," *Adv. Phys.* **63**, 1–76 (2014).
- ⁴A. C. Ferrari, F. Bonaccorso, V. Fal'Ko, K. S. Novoselov, S. Roche, P. Bøggild, S. Borini, F. H. Koppens, V. Palermo, N. Pugno *et al.*, "Science and technology roadmap for graphene, related two-dimensional crystals, and hybrid systems," *Nanoscale* **7**, 4598–4810 (2015).
- ⁵M. Mehboudi, K. Utt, H. Terrones, E. O. Harriss, A. A. Pacheco SanJuan, and S. Barraza-Lopez, "Strain and the optoelectronic properties of nonplanar phosphorene monolayers," *Proc. Natl. Acad. Sci. U.S.A.* **112**, 5888–5892 (2015).

- ⁶J. W. Villanova and K. Park, "Spin textures of topological surface states at side surfaces of Bi_2Se_3 from first principles," *Phys. Rev. B* **93**, 085122 (2016).
- ⁷J. W. Villanova, E. Barnes, and K. Park, "Engineering and probing topological properties of Dirac semimetal films by asymmetric charge transfer," *Nano Lett.* **17**, 963–972 (2017).
- ⁸F. Bonaccorso, Z. Sun, T. Hasan, and A. Ferrari, "Graphene photonics and optoelectronics," *Nat. Photonics* **4**, 611 (2010).
- ⁹Q. Bao, H. Hoh, and Y. Zhang, *Graphene Photonics, Optoelectronics, and Plasmonics* (CRC Press, 2017).
- ¹⁰J. S. Ponraj, Z.-Q. Xu, S. C. Dhanabalan, H. Mu, Y. Wang, J. Yuan, P. Li, S. Thakur, M. Ashrafi, K. Mccoubrey *et al.*, "Photonics and optoelectronics of two-dimensional materials beyond graphene," *Nanotechnology* **27**, 462001 (2016).
- ¹¹M. Liu, X. Yin, E. Ulin-Avila, B. Geng, T. Zentgraf, L. Ju, F. Wang, and X. Zhang, "A graphene-based broadband optical modulator," *Nature* **474**, 64–67 (2011).
- ¹²V. Sorianello, M. Midrio, G. Contestabile, I. Asselberghs, J. Van Campenhout, C. Huyghebaert, I. Goykhman, A. Ott, A. Ferrari, and M. Romagnoli, "Graphene-silicon phase modulators with gigahertz bandwidth," *Nat. Photonics* **12**, 40–44 (2018).
- ¹³R. Hao, J. Jiao, X. Peng, Z. Zhen, R. Dagarbek, Y. Zou, and E. Li, "Experimental demonstration of a graphene-based hybrid plasmonic modulator," *Opt. Lett.* **44**, 2586–2589 (2019).
- ¹⁴Z. Yin, J. Zhu, Q. He, X. Cao, C. Tan, H. Chen, Q. Yan, and H. Zhang, "Graphene-based materials for solar cell applications," *Adv. Energy Mater.* **4**, 1300574 (2014).
- ¹⁵P. O'keeffe, D. Catone, A. Paladini, F. Toschi, S. Turchini, L. Avaldi, F. Martelli, A. Agresti, S. Pescetelli, A. Del Rio Castillo *et al.*, "Graphene-induced improvements of perovskite solar cell stability: Effects on hot-carriers," *Nano Lett.* **19**, 684–691 (2019).
- ¹⁶A. Safaei, S. Chandra, M. W. Shabbir, M. N. Leuenerger, and D. Chanda, "Dirac plasmon-assisted asymmetric hot carrier generation for room-temperature infrared detection," *Nat. Commun.* **10**, 3498 (2019).
- ¹⁷A. Grigorenko, M. Polini, and K. Novoselov, "Graphene plasmonics," *Nat. Photonics* **6**, 749 (2012).
- ¹⁸Y. Fan, N.-H. Shen, F. Zhang, Q. Zhao, H. Wu, Q. Fu, Z. Wei, H. Li, and C. M. Soukoulis, "Graphene plasmonics: A platform for 2D optics," *Adv. Opt. Mater.* **7**, 1800537 (2019).
- ¹⁹F. J. Lopez-Rodriguez and G. G. Naumis, "Analytic solution for electrons and holes in graphene under electromagnetic waves: Gap appearance and nonlinear effects," *Phys. Rev. B* **78**, 201406 (2008).
- ²⁰F. López-Rodríguez and G. Naumis, "Graphene under perpendicular incidence of electromagnetic waves: Gaps and band structure," *Philos. Mag.* **90**, 2977–2988 (2010).
- ²¹O. V. Kibis, "Metal-insulator transition in graphene induced by circularly polarized photons," *Phys. Rev. B* **81**, 165433 (2010).
- ²²H. L. Calvo, H. M. Pastawski, S. Roche, and L. E. F. Torres, "Tuning laser-induced band gaps in graphene," *Appl. Phys. Lett.* **98**, 232103 (2011).
- ²³D. Sun, G. Aivazian, A. M. Jones, J. S. Ross, W. Yao, D. Cobden, and X. Xu, "Ultrafast hot-carrier-dominated photocurrent in graphene," *Nat. Nanotechnol.* **7**, 114 (2012).
- ²⁴K. Kristinsson, O. V. Kibis, S. Morina, and I. A. Shelykh, "Control of electronic transport in graphene by electromagnetic dressing," *Sci. Rep.* **6**, 20082 (2016).
- ²⁵I. V. Iorsh, K. Dini, O. V. Kibis, and I. A. Shelykh, "Optically induced Lifshitz transition in bilayer graphene," *Phys. Rev. B* **96**, 155432 (2017).
- ²⁶O. Kibis, K. Dini, I. Iorsh, and I. Shelykh, "All-optical band engineering of gapped Dirac materials," *Phys. Rev. B* **95**, 125401 (2017).
- ²⁷O. Kibis, K. Dini, I. Iorsh, V. Dragunov, and I. Shelykh, "Electromagnetic dressing of graphene," *J. Struct. Chem.* **59**, 867–869 (2018).
- ²⁸R. Wang, B. Wang, R. Shen, L. Sheng, and D. Y. Xing, "Floquet Weyl semimetal induced by off-resonant light," *Europhys. Lett.* **105**, 17004 (2014).
- ²⁹A. Narayan, "Floquet dynamics in two-dimensional semi-Dirac semimetals and three-dimensional Dirac semimetals," *Phys. Rev. B* **91**, 205445 (2015).

- ³⁰C.-K. Chan, N. H. Lindner, G. Refael, and P. A. Lee, "Photocurrents in Weyl semimetals," *Phys. Rev. B* **95**, 041104 (2017).
- ³¹G. G. Naumis, S. Barraza-Lopez, M. Oliva-Leyva, and H. Terrones, "Electronic and optical properties of strained graphene and other strained 2D materials: A review," *Rep. Prog. Phys.* **80**, 096501 (2017).
- ³²R. Carrillo-Bastos and G. G. Naumis, "Band gaps and wavefunctions of electrons coupled to pseudo electromagnetic waves in rippled graphene," *Phys. Status Solidi RRL* **12**, 1800072 (2018).
- ³³T. Higuchi, C. Heide, K. Ullmann, H. B. Weber, and P. Hommelhoff, "Light-field-driven currents in graphene," *Nature* **550**, 224–228 (2017).
- ³⁴E. G. Mishchenko, "Effect of electron-electron interactions on the conductivity of clean graphene," *Phys. Rev. Lett.* **98**, 216801 (2007).
- ³⁵S. A. Herrera and G. G. Naumis, "Electronic and optical conductivity of Kekulé-patterned graphene: Intravalley and intervalley transport," *Phys. Rev. B* **101**, 205413 (2020).
- ³⁶B. Mielnik and D. J. Fernández C., "An electron trapped in a rotating magnetic field," *J. Math. Phys.* **30**, 537–549 (1989).
- ³⁷B. Mielnik and C. David J. Fernández, "Is there an instability transition in standing wave traps?," *Lett. Math. Phys.* **17**, 87–94 (1989).
- ³⁸M. Goerbig, J.-N. Fuchs, G. Montambaux, and F. Piéchon, "Tilted anisotropic Dirac cones in quinoid-type graphene and α -(BEDT-TTF)₂I₃," *Phys. Rev. B* **78**, 045415 (2008).
- ³⁹B. Feng, J. Zhang, S. Ito, M. Arita, C. Cheng, L. Chen, K. Wu, F. Komori, O. Sugino, K. Miyamoto, T. Okuda, S. Meng, and I. Matsuda, "Discovery of 2D anisotropic Dirac cones," *Adv. Mater.* **30**, 1704025 (2018).
- ⁴⁰M. Mehboudi, A. M. Dorio, W. Zhu, A. van der Zande, H. O. Churchill, A. A. Pacheco-Sanjuan, E. O. Harriss, P. Kumar, and S. Barraza-Lopez, "Two-dimensional disorder in black phosphorus and monochalcogenide monolayers," *Nano Lett.* **16**, 1704–1712 (2016).
- ⁴¹K. L. Utt, P. Rivero, M. Mehboudi, E. O. Harriss, M. F. Borunda, A. A. Pacheco SanJuan, and S. Barraza-Lopez, "Intrinsic defects, fluctuations of the local shape, and the photo-oxidation of black phosphorus," *ACS Cent. Sci.* **1**, 320–327 (2015).
- ⁴²S. P. Poudel, J. W. Villanova, and S. Barraza-Lopez, "Group-IV monochalcogenide monolayers: Two-dimensional ferroelectrics with weak intralayer bonds and a phosphorene like monolayer dissociation energy," *Phys. Rev. Mater.* **3**, 124004 (2019).
- ⁴³S. W. Jung, S. H. Ryu, W. J. Shin, Y. Sohn, M. Huh, R. J. Koch, C. Jozwiak, E. Rotenberg, A. Bostwick, and K. S. Kim, "Black phosphorus as a bipolar pseudospin semiconductor," *Nat. Mater.* **19**, 277 (2020).
- ⁴⁴S. Verma, A. Mawrie, and T. K. Ghosh, "Effect of electron-hole asymmetry on optical conductivity in 8-*Pmmn* borophene," *Phys. Rev. B* **96**, 155418 (2017).
- ⁴⁵A. E. Champo and G. G. Naumis, "Metal-insulator transition in 8-*Pmmn* borophene under normal incidence of electromagnetic radiation," *Phys. Rev. B* **99**, 035415 (2019).
- ⁴⁶I. Boustani, "New quasi-planar surfaces of bare boron," *Surf. Sci.* **370**, 355–363 (1997).
- ⁴⁷Z. Zhang, E. S. Penev, and B. I. Yakobson, "Two-dimensional boron: Structures, properties and applications," *Chem. Soc. Rev.* **46**, 6746–6763 (2017).
- ⁴⁸A. J. Mannix, Z. Zhang, N. P. Guisinger, B. I. Yakobson, and M. C. Hersam, "Borophene as a prototype for synthetic 2D materials development," *Nat. Nanotechnol.* **13**, 444–450 (2018).
- ⁴⁹A. D. Zabolotskiy and Y. E. Lozovik, "Strain-induced pseudomagnetic field in the Dirac semimetal borophene," *Phys. Rev. B* **94**, 165403 (2016).
- ⁵⁰V. Ibarra-Sierra, J. Sandoval-Santana, A. Kunold, and G. G. Naumis, "Dynamical band gap tuning in anisotropic tilted Dirac semimetals by intense elliptically polarized normal illumination and its application to 8-*Pmmn* borophene," *Phys. Rev. B* **100**, 125302 (2019).
- ⁵¹T. Dittrich, P. Hänggi, G.-L. Ingold, B. Kramer, G. Schön, and W. Zwerger, *Quantum Transport and Dissipation* (Wiley-VCH, Weinheim, 1998), Vol. 3.
- ⁵²C. D. J. Fernandez, M. A. del Olmo, and M. Santander, "Orbital Aharonov-Anandan geometric phase for confined motion in a precessing magnetic field," *J. Phys. A: Math. Gen.* **25**, 6409–6418 (1992).
- ⁵³S. C. Y. Cruz and B. Mielnik, "Non-inertial quantization: Truth or illusion?," in *Journal of Physics: Conference Series* (IOP Publishing, 2016), Vol. 698, p. 012002.
- ⁵⁴H. Hübener, M. A. Sentef, U. De Giovannini, A. F. Kemper, and A. Rubio, "Creating stable Floquet-Weyl semimetals by laser-driving of 3D Dirac materials," *Nat. Commun.* **8**, 13940 (2017).
- ⁵⁵A. Iurov, L. Zhemchuzhna, G. Gumbs, and D. Huang, "Exploring interacting Floquet states in black phosphorus: Anisotropy and bandgap laser tuning," *J. Appl. Phys.* **122**, 124301 (2017).
- ⁵⁶M. Rodriguez-Vega, M. Lentz, and B. Seradjeh, "Floquet perturbation theory: Formalism and application to low-frequency limit," *New J. Phys.* **20**, 093022 (2018).
- ⁵⁷A. Iurov, G. Gumbs, and D. Huang, "Peculiar electronic states, symmetries, and berry phases in irradiated α -t₃ materials," *Phys. Rev. B* **99**, 205135 (2019).
- ⁵⁸T. Oka and S. Kitamura, "Floquet engineering of quantum materials," *Annu. Rev. Condens. Matter Phys.* **10**, 387–408 (2019).
- ⁵⁹M. Vogl, P. Laurell, A. D. Barr, and G. A. Fiete, "Flow equation approach to periodically driven quantum systems," *Phys. Rev. X* **9**, 021037 (2019).
- ⁶⁰M. Vogl, M. Rodriguez-Vega, and G. A. Fiete, "Effective Floquet Hamiltonian in the low-frequency regime," *Phys. Rev. B* **101**, 024303 (2020).
- ⁶¹M. Vogl, M. Rodriguez-Vega, and G. A. Fiete, "Effective Floquet Hamiltonians for periodically driven twisted bilayer graphene," *Phys. Rev. B* **101**, 235411 (2020).
- ⁶²S. A. Herrera and G. G. Naumis, "Kubo conductivity for anisotropic tilted Dirac semimetals and its application to 8-*Pmmn* borophene: Role of frequency, temperature, and scattering limits," *Phys. Rev. B* **100**, 195420 (2019).
- ⁶³B. Dey and T. K. Ghosh, "Photoinduced valley and electron-hole symmetry breaking in α -T₃ lattice: The role of a variable berry phase," *Phys. Rev. B* **98**, 075422 (2018).
- ⁶⁴W. Magnus and S. Winkler, *Hill's Equation* (Courier Corporation, 2013).
- ⁶⁵K. M. Urwin and F. Arscott, "III.—Theory of the Whittaker Hill equation," *Proc. R. Soc. Edinburgh Sect. A: Math.* **69**, 28–44 (1970).
- ⁶⁶C. Ziener, M. Rückl, T. Kampf, W. Bauer, and H. Schlemmer, "Mathieu functions for purely imaginary parameters," *J. Comput. Appl. Math.* **236**, 4513–4524 (2012).
- ⁶⁷J. Lachapelle and R. H. Brandenberger, "Preheating with non-standard kinetic term," *J. Cosmol. Astropart. Phys.* **2009**, 020–020.
- ⁶⁸Y. Zhou and M. W. Wu, "Optical response of graphene under intense terahertz fields," *Phys. Rev. B* **83**, 245436 (2011).
- ⁶⁹M. Bukov, L. D'Alessio, and A. Polkovnikov, "Universal high-frequency behavior of periodically driven systems: From dynamical stabilization to Floquet engineering," *Adv. Phys.* **64**, 139–226 (2015).
- ⁷⁰V. Gritsev and A. Polkovnikov, "Integrable Floquet dynamics," *SciPost Phys.* **2**, 021 (2017).
- ⁷¹J. C. Sandoval-Santana, V. G. Ibarra-Sierra, J. L. Cardoso, A. Kunold, P. Roman-Taboada, and G. Naumis, "Method for finding the exact effective Hamiltonian of time-driven quantum systems," *Ann. Phys.* **531**, 1900035 (2019).
- ⁷²C. Heide, T. Higuchi, H. B. Weber, and P. Hommelhoff, "Coherent electron trajectory control in graphene," *Phys. Rev. Lett.* **121**, 207401 (2018).
- ⁷³D. Wu, J. Guo, J. Du, C. Xia, L. Zeng, Y. Tian, Z. Shi, Y. Tian, X. J. Li, Y. H. Tsang, and J. Jie, "Highly polarization-sensitive, broadband, self-powered photodetector based on graphene/PdSe₂/germanium heterojunction," *ACS Nano* **13**, 9907–9917 (2019).
- ⁷⁴M. W. Kudenov, J. L. Pezzaniti, and G. R. Gerhart, "Microbolometer-infrared imaging Stokes polarimeter," *Opt. Eng.* **48**(6), 063201 (2009).
- ⁷⁵G. Myhre, W.-L. Hsu, A. Peinado, C. LaCasse, N. Brock, R. A. Chipman, and S. Pau, "Liquid crystal polymer full-Stokes division of focal plane polarimeter," *Opt. Express* **20**, 27393–27409 (2012).
- ⁷⁶J. S. Tyo, D. L. Goldstein, D. B. Chenault, and J. A. Shaw, "Review of passive imaging polarimetry for remote sensing applications," *Appl. Opt.* **45**, 5453–5469 (2006).